Monthly Notices
of the
ROYAL ASTRONOMICAL SOCIETY

MNRAS **433,** 498–505 (2013)
Advance Access publication 2013 May 21

doi:10.1093/mnras/stt741

Large gas reservoirs and free–free emission in two lensed star-forming galaxies at $z = 2.7$

M. Aravena,[1⋆] E. J. Murphy,[2] J. E. Aguirre,[3] M. L. N. Ashby,[4] B. A. Benson,[5,6] M. Bothwell,[7,8] M. Brodwin,[9] J. E. Carlstrom,[5,6,10,11,12] S. C. Chapman,[13,14] T. M. Crawford,[5,11] C. de Breuck,[1] C. D. Fassnacht,[15] A. H. Gonzalez,[16] T. R. Greve,[17] B. Gullberg,[1] Y. Hezaveh,[18] G. P. Holder,[18] W. L. Holzapfel,[19] R. Keisler,[5,10] M. Malkan,[20] D. P. Marrone,[7] V. McIntyre,[21] C. L. Reichardt,[19] K. Sharon,[5,11] J. S. Spilker,[7] B. Stalder,[4,22] A. A. Stark,[4] J. D. Vieira[23] and A. Weiß[24]

[1]*European Southern Observatory, Alonso de Cordova 3107, Casilla 19001, Vitacura Santiago, Chile*
[2]*Observatories of the Carnegie Institution for Science, 813 Santa Barbara Street, Pasadena, CA 91101, USA*
[3]*University of Pennsylvania, 209 South 33rd Street, Philadelphia, PA 19104, USA*
[4]*Harvard–Smithsonian Center for Astrophysics, 60 Garden Street, Cambridge, MA 02138, USA*
[5]*Kavli Institute for Cosmological Physics, University of Chicago, 5640 South Ellis Avenue, Chicago, IL 60637, USA*
[6]*Enrico Fermi Institute, University of Chicago, 5640 South Ellis Avenue, Chicago, IL 60637, USA*
[7]*Steward Observatory, University of Arizona, 933 North Cherry Avenue, Tucson, AZ 85721, USA*
[8]*Cavendish Laboratory, University of Cambridge, 19 JJ Thomson Avenue, Cambridge CB3 0HE, UK*
[9]*Department of Physics and Astronomy, University of Missouri, 5110 Rockhill Road, Kansas City, MO 64110, USA*
[10]*Department of Physics, University of Chicago, 5640 South Ellis Avenue, Chicago, IL 60637, USA*
[11]*Department of Astronomy and Astrophysics, University of Chicago, 5640 South Ellis Avenue, Chicago, IL 60637, USA*
[12]*Argonne National Laboratory, 9700 S. Cass Avenue, Argonne, IL 60439, USA*
[13]*Institute of Astronomy, University of Cambridge, Madingley Road, Cambridge CB3 0HA, UK*
[14]*Dalhousie University, Halifax, Nova Scotia B3H 4R2, Canada*
[15]*Department of Physics, University of California, One Shields Avenue, Davis, CA 95616, USA*
[16]*Department of Astronomy, University of Florida, Gainesville, FL 32611, USA*
[17]*Department of Physics and Astronomy, University College London, Gower Street, London WC1E 6BT, UK*
[18]*Department of Physics, McGill University, 3600 Rue University, Montreal, Quebec H3A 2T8, Canada*
[19]*Department of Physics, University of California, Berkeley, CA 94720, USA*
[20]*Department of Physics and Astronomy, University of California, Los Angeles, CA 90095-1547, USA*
[21]*Australia Telescope National Facility, CSIRO, Epping, NSW 1710, Australia*
[22]*Department of Physics, Harvard University, 17 Oxford Street, Cambridge, MA 02138, USA*
[23]*California Institute of Technology, 1200 E. California Blvd., Pasadena, CA 91125, USA*
[24]*Max-Planck-Institut für Radioastronomie, Auf dem Hügel 69, D-53121 Bonn, Germany*

Accepted 2013 April 26. Received 2013 April 5; in original form 2013 February 13

ABSTRACT

We report the detection of CO(1–0) line emission in the bright, lensed star-forming galaxies SPT-S 233227−5358.5 ($z = 2.73$) and SPT-S 053816−5030.8 ($z = 2.78$), using the Australia Telescope Compact Array. Both galaxies were discovered in a large-area millimetre survey with the South Pole Telescope (SPT) and found to be gravitationally lensed by intervening structures. The measured CO intensities imply galaxies with molecular gas masses of $(3.2 \pm 0.5) \times 10^{10}(\mu/15)^{-1}(X_{\rm CO}/0.8)$ and $(1.7 \pm 0.3) \times 10^{10}(\mu/20)^{-1}(X_{\rm CO}/0.8)\,{\rm M}_\odot$, and gas depletion time-scales of $4.9 \times 10^7(X_{\rm CO}/0.8)$ and $2.6 \times 10^7(X_{\rm CO}/0.8)$ yr, respectively, where μ corresponds to the lens magnification and $X_{\rm CO}$ is the CO luminosity to gas mass conversion factor. In the case of SPT-S 053816−5030.8, we also obtained significant detections of the rest-frame 115.7 and 132.4 GHz radio continuum. Based on the radio-to-infrared spectral energy distribution and an assumed synchrotron spectral index, we find that 42 ± 10 and 55 ±

⋆E-mail: maravena@eso.org

13 per cent of the flux at rest-frame 115.7 and 132.4 GHz arises from free–free emission. We find a radio-derived intrinsic star formation rate of $470 \pm 170\,M_\odot\ yr^{-1}$, consistent within the uncertainties with the infrared estimate. Based on the morphology of this object in the source plane, the derived gas mass and the possible flattening of the radio spectral index towards low frequencies, we argue that SPT-S 053816−5030.8 exhibits properties compatible with a scaled-up local ultraluminous infrared galaxy.

Key words: galaxies: evolution – galaxies: formation – galaxies: high-redshift – galaxies: starburst – cosmology: observations.

1 INTRODUCTION

Submillimetre/millimetre blank field surveys have uncovered a significant population of dusty star-forming galaxies (DSFGs) at cosmological distances. These galaxies are found to harbour intense star formation activity, with typical star formation rates (SFRs) $> 500\,M_\odot\ yr^{-1}$, and to be generally located at $z > 1$ (Blain et al. 2002; Chapman et al. 2005; Lagache, Puget & Dole 2005; Vieira et al. 2013; Weiss et al. 2013). Their observational properties suggest that they are the likely progenitors of local massive early-type galaxies, and they appear to trace large galaxy overdensities at high redshifts (Brodwin et al. 2008; Daddi et al. 2009; Viero et al. 2009; Aravena et al. 2010; Amblard et al. 2011; Capak et al. 2011).

The interstellar medium (ISM) plays a critical role in shaping the overall evolution of galaxies as it constitutes the primary reservoir of material for star formation. The continuous interaction between stars and the ISM governs the overall and chemical composition of galaxies. The molecular gas in the ISM is mostly composed of H_2 and He, with a minor fraction ($\sim$1 per cent) of other molecules and dust. However, H_2 is difficult to detect in the cold molecular ISM. The CO molecule, particularly in its lowest rotational transition $J = 1-0$, represents the best tracer of H_2, specifically its mass and spatial distribution (e.g. Omont 2007).

Large efforts have been devoted to investigating the physical properties of DSFGs. However, due to their faintness and large cosmological distances, only a handful have been targeted in a sufficiently large number of molecular gas emission lines (e.g. CO) to allow for a full characterization of their ISM. Follow-up CO studies have been focused on the observation of $J \geq 3$ CO transitions. However, CO(1–0) observations in a few unlensed DSFGs indicate that the gas masses are two times larger and up to three times more spatially extended than expected based on $J \geq 3$ CO transitions, heavily altering our understanding of these systems (e.g. Papadopoulos & Ivison 2002; Greve, Ivison & Papadopoulos 2003; Harris et al. 2010; Ivison et al. 2011; Riechers et al. 2011). This highlights the need for low-J CO observations.

Strongly lensed systems, including IRAS F10214+4722, the Cloverleaf, the Cosmic Eyelash and SMM 02399−0136, have proven to be a boon for studies of far-infrared (IR) and millimetre line studies at high redshift (e.g. Brown & Vanden Bout 1991, 1992; Rowan-Robinson et al. 1991; Barvainis, Antonucci & Coleman 1992; Frayer et al. 1998; Ivison et al. 1998; Solomon & Vanden Bout 2005; Swinbank et al. 2010). The recent discovery of a population of gravitationally lensed, highly magnified, star-forming galaxies in the >100 square degree millimetre and far-IR surveys carried out by the South Pole Telescope (SPT; Carlstrom et al. 2011) and the *Herschel Space Observatory* (Pilbratt et al. 2010) has provided a remarkable opportunity to study in great detail the process of star formation and conditions of the ISM in this cosmologically important population of galaxies (Negrello et al. 2010; Vieira et al. 2010, 2013).

We have started a systematic follow-up campaign with the Australia Telescope Compact Array (ATCA) to study the molecular gas content in a sample of gravitationally lensed star-forming galaxies through the observation of $J \leq 2$ CO emission. These galaxies were found in the 1.4–3 mm wavelength sky maps produced by the SPT Sunyaev–Zel'dovich effect survey and have accurate spectroscopic redshifts (Greve et al. 2012). In this work, we report pilot observations of the CO(1–0) line emission in two such sources. Hereafter, we adopt a Λ cold dark matter cosmology with $H_0 = 71\,km\,s^{-1}\,Mpc^{-1}$, $\Omega_M = 0.27$ and $\Omega_\Lambda = 0.73$.

2 OBSERVATIONS

2.1 SPT sources

The two targets of this work, SPT-S 233227−5358.5 and SPT-S 053816−5030.8 (hereafter SPT 2332−53 and SPT 0538−50), were the first dusty-spectrum SPT sources (Vieira et al. 2010) to have spectroscopic redshift measurements. In both cases, a redshift determination was obtained through the identification of CO and [CI] line emission in wide-band submillimetre spectra obtained with the Z-spec instrument on the Atacama Pathfinder Experiment (APEX) 12 m telescope, and confirmed with optical spectroscopy obtained with the Very Large Telescope. The redshifts derived for the lensed objects are $z = 2.738$ and 2.783 for SPT 2332−53 and SPT 0538−50, respectively (Greve et al. 2012). Both galaxies are associated with faint *Spitzer* Infrared Array Camera (IRAC) 4.5 μm sources (Fig. 1), and are detected with the Large APEX Bolometer Camera (LABOCA) and the Submillimetre APEX Bolometer Camera (SABOCA) at 870 and 350 μm, respectively (see Greve et al. 2012).

As shown by the 850 and 350 μm images (fig. 1 in Greve et al. 2012), the submillimetre emission in SPT 2332−53 is resolved into six major components, three of which are detected at 350 μm (A, B and C; Fig. 1). A massive foreground galaxy cluster at $z = 0.403$ is identified as the gravitational lens for this source (Greve et al. 2012). A full analysis of the lensing structure of this object will be presented in Vieira et al. (in preparation). That work leads to a magnification factor in the range $\mu = 10-20$, and thus we adopt $\mu = 15 \pm 5$ throughout.

SPT 0538−50 is unresolved in the LABOCA and SABOCA images. Recent Atacama Large Millimeter/submillimeter Array (ALMA) 850 μm sub-arcsecond imaging of this source shows an Einstein ring around a foreground galaxy at $z = 0.443$, confirming the gravitational lensed nature of this source (Hezaveh et al. 2013). A detailed lens model gives a magnification $\mu = 20 \pm 4$ (Hezaveh et al. 2013). Unless otherwise stated, the quoted uncertainties in the magnification factors for both sources are not propagated to the observed quantities throughout.

Greve et al. (2012) find observed IR luminosities $L_{IR}(8–1000\,\mu m) = (6.5 \pm 1.6) \times 10^{13}\,L_\odot$ for both sources.

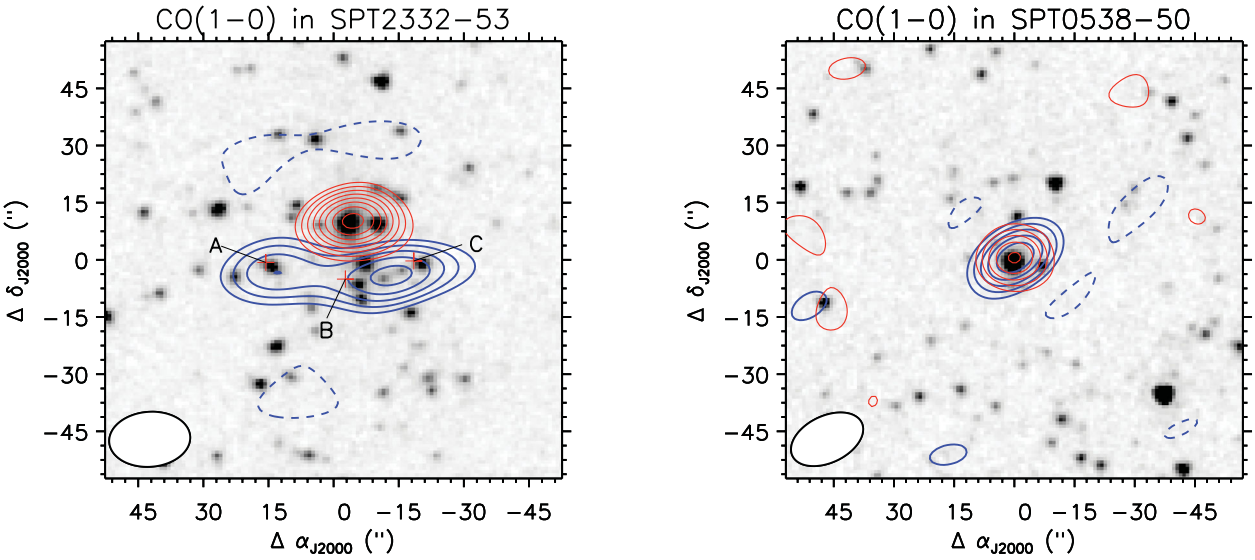

Figure 1. CO(1–0) and 35 GHz continuum detections towards SPT 2332−53 and SPT 0538−50. The *Spitzer* IRAC 4.5 μm image is shown in grey-scale with blue contours overlaid representing the CO(1–0) line emission (dirty image) averaged over 350 and 220 km s^{-1}, respectively. These contours are in steps of $\pm1\sigma$, starting at $\pm2\sigma$, with $\sigma = 0.32$ and 0.44 mJy beam^{-1}, respectively. The red contours represent the 35 GHz continuum emission (dirty image), and are shown in steps of $+1\sigma$, starting at $+2\sigma$, with $\sigma = 31$ and 21 μJy beam^{-1}, respectively. For SPT 2332−53, the location of the SABOCA sources is shown as red plus symbols, following the notation from Greve et al. (2012). The axes show the offset, in arcseconds, with respect to the phase tracking centre.

However, recent *Herschel* far-IR data lead to an improved observed IR luminosity of $(8.8 \pm 1.3) \times 10^{13}\,L_\odot$ for SPT 0538−50 (Hezaveh et al. 2013). The revised value for the IR luminosity of SPT 2332−53 is well within uncertainties with the estimate from Greve et al. (2012), and we use this value throughout. From this, we adopt intrinsic IR luminosities of $(4.3 \pm 1.1) \times 10^{12}(\mu/15)^{-1}$ and $(4.4 \pm 0.65) \times 10^{12}(\mu/20)^{-1}\,L_\odot$ for SPT 2332−53 and SPT 0538−50, respectively. The estimated total IR luminosities are derived from fitting a single-temperature grey-body model to the data at $\lambda_{\rm rest} > 50$ μm, and thus do not account for a possible hot dust component (see Greve et al. 2012 for details). While such hot dust component would increase the actual IR luminosities of our targets, such emission would likely arise from AGN and thus would not strictly trace the star formation in the host galaxies, being irrelevant for the analysis below.

2.2 ATCA CO data

We used ATCA in the H75 compact-array configuration to observe the redshifted CO(1–0) emission line ($\nu_{\rm rest} = 115.271$ GHz) in the two star-forming galaxies SPT 2332−53 and SPT 0538−50. The observations were performed between UT 2012 July 27 and 30 under good weather conditions with five working antennas, and the sources were observed for ∼10 h each.

We used the Compact Array Broadband Backend (CABB) configured in the 1 M-0.5 k mode, which leads to a bandwidth of 2 GHz per correlator window with 1 MHz per channel of spectral resolution. In both cases, one of the windows was tuned to 35 000 MHz to obtain a measurement of the continuum emission. For SPT 2332−53 the other window was tuned to 31 412 MHz, and for SPT 0538−50 this was tuned to 30 600 MHz. The phase tracking centres were $\alpha_{2000} = 23^{\rm h}32^{\rm m}27\overset{\rm s}{.}8$, $\delta_{2000} = -53^\circ\,58'37''$, and $\alpha_{2000} = 05^{\rm h}38^{\rm m}16\overset{\rm s}{.}8$, $\delta_{2000} = -50^\circ\,30'52''$, respectively, based on the prior positions obtained with LABOCA at 870 μm.

The bright quasars 2355−534 ($S_{35\,\rm GHz} \sim 1.8$ Jy) and 0537−441 ($S_{35\,\rm GHz} \sim 6.2$ Jy) were observed every 6–7 min for gain calibration, and every ∼1 h for pointing calibration. The sources 1921−293 (∼14 Jy) and 0537−441 were used for bandpass calibration, and Uranus and 1934−638 were used as amplitude calibrators. The software package MIRIAD (Sault, Teuben & Wright 1995) and the Common Astronomy Software Applications (McMullin et al. 2007) were used for editing, calibration and imaging. Absolute flux calibration is estimated to be accurate to within 15 per cent. Flagging of visibilities was performed for the case of SPT 0538−50, where some channels fell close to the edge of the *Q*-band short-frequency limit at 30 GHz. The visibilities were inverted using natural weighting yielding synthesized beam sizes for SPT 2332−53 and SPT 0538−50 of 21.8 arcsec × 16.8 arcsec and 22.2 arcsec × 13.9 arcsec (at ∼31 GHz), and 19.2 arcsec × 14.8 arcsec and 18.0 arcsec × 14.2 arcsec (at 35 GHz), respectively. The final data result in an rms of 0.70 mJy beam^{-1} per 4 MHz (39 km s^{-1}) channel at ∼31.4 GHz and 0.60 mJy beam^{-1} per 2 MHz (19.7 km s^{-1}) channel at ∼30.6 GHz for SPT 2332−53 and SPT 0538−50. We reach continuum rms levels of 40 and 35 μJy beam^{-1} at 31.4 and 35 GHz, respectively, for SPT 2332−53, and 35 and 20 μJy beam^{-1} at 30.6 and 35 GHz, respectively, for SPT 0538−50.

2.3 ATCA low-frequency data

ATCA observations at 2.2, 5.5 and 9.0 GHz of SPT 2332−53 and SPT 0538−50 were made between UT 2012 January 23 and 27 using the CABB in the 1M-0.5k mode (see above). The observations were performed in the most extended ATCA configuration, 6A, with six working antennas. The data were edited, calibrated and imaged using the MIRIAD package. Data affected by known radio frequency interference or with bad visibility ranges were flagged accordingly. We estimate an absolute calibration uncertainty of ∼5 per cent at 2.2 and 5.5 GHz, and 10 per cent at 9.0 GHz. We inverted the visibilities using natural weighting leading to beam sizes of ∼7.7 arcsec × 5.2 arcsec, 3.2 arcsec × 2.1 arcsec and 2.0 arcsec × 1.3 arcsec at 2.2, 5.5 and 9.0 GHz, respectively. For

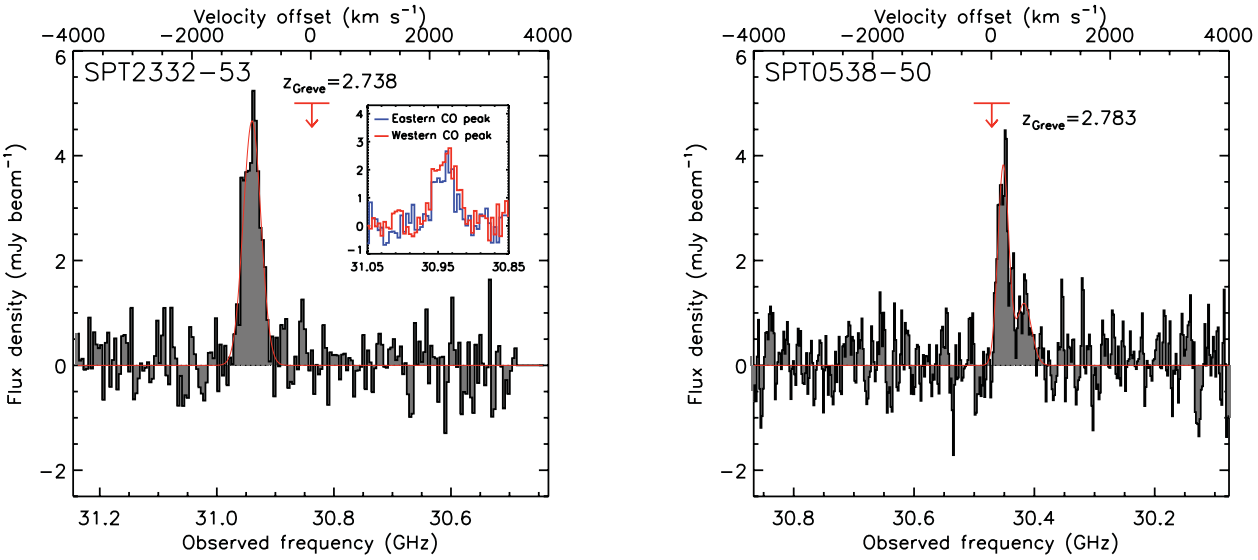

Figure 2. ATCA spectra of the CO(1–0) line emission towards SPT 2332−53 and SPT 0538−50. Their spectra are shown at 39 km s^{-1} (4 MHz) and 20 km s^{-1} (2 MHz) resolution, respectively, and centred at the redshift determined by Greve et al. (2012). A solid red line shows a two-component Gaussian fitting to the CO profiles in each case. The inset plot for SPT 2232−52 shows the comparison of the CO profiles for the eastern and western components.

SPT 2332−53, we reach rms noise values of 200, 500 and 100 μJy beam^{-1} at 2.2, 5.5 and 9.0 GHz, respectively. For SPT 0538−50, we reach rms noise values of 200, 100 and 75 μJy beam^{-1} at each frequency, respectively.

3 RESULTS

3.1 SPT 2332−53

The CO(1–0) line towards SPT 2332−53 is well detected and spatially resolved into two main peaks separated by ∼30 arcsec (Fig. 1). The CO profiles of both peaks (east and west) are coincident in frequency and line shape suggesting that they arise from the same lensed background object (Fig. 2). A comparison with the SABOCA image from Greve et al. (2012) indicates that the CO distribution corresponds to the blended IR components A, B and C, following the nomenclature adopted by Greve et al.

The continuum emission was measured from the 35 GHz correlator window and the line-free channels at ∼31.4 GHz. We find significant detections at both frequencies from a source located at ∼15 arcsec to the north of the CO emission, with flux densities $S_{31.4\,\mathrm{GHz}} = 310 \pm 40$ μJy and $S_{35\,\mathrm{GHz}} = 300 \pm 35$ μJy (Fig. 1). This source is identified with the brightest cluster galaxy (BCG) in the foreground structure. It is detected at 3.4 and 4.6 μm with *Spitzer* IRAC, though not at 12 and 22 μm with the *Wide-field Infrared Survey Explorer*. This source is also detected in the 5.5 and 9.0 GHz ATCA images. The non-detection of continuum at the CO position yields a limit to the integrated ∼35 GHz flux density of the background source of < 220 μJy (3σ with respect to the zero level).

From Gaussian fitting to the CO profile of the combined emission from both components (Fig. 2), we find the fluxes and line widths listed in Table 1. The total line intensity is obtained by creating a moment-0 image, integrated over ∼600 km s^{-1} around the line (Table 1).

3.2 SPT 0538−50

The CO(1–0) line towards SPT 0538−50 is also significantly detected; however, at the spatial resolution of these observations, the source is unresolved (Fig. 1). The spectrum suggests the existence of two CO line peaks (Fig. 2). Fitting a two-component Gaussian profile to the spectrum, we find the bright (SPT 0538−50blue) and weak (SPT 0538−50red) CO components separated by 350 ± 50 km s^{-1} in velocity. The fainter CO component carries ≈30 per cent of

Table 1. Observed CO properties.

Source	z_{CO} [a]	S_{CO} [b] (mJy)	v_{FWHM} [b] (km s^{-1})	$I_{\mathrm{CO\,1-0}}$ [c] (Jy km s^{-1})	L'_{CO} [d] ($\times 10^{10}\,(\mu/\mu_0)^{-1}$ K km s^{-1} pc^2)	$S_{31\,\mathrm{GHz}}$ [e] (μJy)	$S_{35\,\mathrm{GHz}}$ [e] (μJy)
SPT 2332−53†	2.7256(2)	4.66 ± 0.51	342 ± 42	1.70 ± 0.25	3.94 ± 0.58	<120	<120
SPT 0538−50blue‡	2.7854(1)	3.81 ± 0.36	210 ± 34	0.85 ± 0.08	1.49 ± 0.14	–	–
SPT 0538−50red‡	2.7897(6)	1.18 ± 0.27	281 ± 80	0.35 ± 0.18	0.61 ± 0.31	–	–
SPT 0538−50	2.7855(1)	–	–	1.20 ± 0.20	2.16 ± 0.36	171 ± 35	130 ± 20

†Integrated values over all CO components are listed.
‡Here, SPT 0538−50blue and SPT 0538−50red are the brighter and fainter CO peaks, respectively.
[a]CO redshift. For SPT 0538−50, the redshift is computed as the weighted average between the redshifts of SPT 0538−50blue and red.
[b]CO line peak flux and line full-width half-maximum (FWHM) velocity.
[c]Integrated CO line intensity ($I_{\mathrm{CO}} = \int S_{\mathrm{CO}} dv$).
[d]CO line luminosity. The magnification factor μ_0 is assumed to be 15 and 20 for SPT 2332−53 and SPT 0538−50, respectively.
[e]Continuum fluxes at ∼31 and 35 GHz.

the CO intensity. Table 1 summarizes the measurements for these sources. We measure the total CO line intensity from the moment-0 image, integrated over 710 km s^{-1} containing both CO line peaks (SPT 0538−50; Table 1).

Continuum emission at 30.6 and 35 GHz is also detected (Fig. 1). In this case, the continuum peak position coincides within 1.0 arcsec of the location of the CO peak. The origin of this emission is discussed in the next sections. Continuum emission is also detected at 2.2 and 5.5 GHz, with flux densities of $S_{2.2\,\mathrm{GHz}} = 650 \pm 200$ μJy and $S_{5.5\,\mathrm{GHz}} = 550 \pm 100$ μJy, respectively. This source is not detected in our 9.0 GHz data, resulting in a 3σ upper limit of 225 μJy (respect to the zero level).

4 ANALYSIS

4.1 The nature of the SPT sources

The results of the source reconstruction of SPT 2332−53 do not allow us to discern whether this object corresponds to a disc galaxy or merger (Vieira et al., in preparation). The CO profile shape, however, does not show evidence for a double-peak structure (Fig. 2) as would be expected for a disc geometry extended on scales of ∼5−10 kpc (Daddi et al. 2010) or for an early-stage merging system (e.g. Greve et al. 2005). This suggests that the molecular gas is distributed over a relatively compact disc or a compact spherical distribution, as in an advanced merger stage, with most of the gas within a radius ∼1–2 kpc.

In the case of SPT 0538−50, the lens reconstruction shows that this source is composed of two components (see Hezaveh et al. 2013): a compact source with a radius of 0.5 ± 0.1 kpc and an extended source with a radius of 1.6 ± 0.3 kpc. The two components appear to spatially overlap, leaving it unclear whether the system corresponds to two interacting galaxies or a clumpy disc with a bright compact source. However, the fraction of the ALMA 870 μm flux distributed between both components, ∼70 per cent of the total L_{IR} for the compact source and ∼30 per cent for the extended one (Hezaveh et al. 2013), is in good agreement with the CO luminosity budget. The brighter CO component (SPT 0538−50blue) carries a luminosity $L'_{\mathrm{CO}} = 1.49 \times 10^{10}\,(\mu/20)^{-1}$ K km s^{-1} pc^2 or ∼70 per cent of the total CO luminosity, while the fainter CO component (SPT 0538−50, red) has a CO luminosity $L'_{\mathrm{CO}} = 6.1 \times 10^{9}\,(\mu/20)^{-1}$ K km s^{-1} pc^2 or ∼30 per cent. This suggests that the compact reconstructed source could be identified with the bright CO line component, while the extended source could be associated with the fainter, broader CO line component (Fig. 2). However, this IR to CO line association remains uncertain. The only way to confirm this is through spatially resolved CO spectroscopy.

4.2 Gas and dynamical masses

The molecular gas mass, M_{gas}, is commonly computed from the CO(1–0) line luminosity using the relation $M_{\mathrm{gas}} = X_{\mathrm{CO}} L'_{\mathrm{CO}}$, where X_{CO} is the CO luminosity to gas mass conversion factor. Its value can vary from galaxy to galaxy, and even within galaxies (e.g. Genzel et al. 2012). We adopt $X_{\mathrm{CO}} = 0.8\,\mathrm{M}_\odot$ (K km s^{-1} pc^2)$^{-1}$, as found for local ultraluminous infrared galaxies (ULIRGs; Downes & Solomon 1998). While this value is typically used for dusty starburst galaxies at high redshift, higher values have been recently found for distant disc galaxies ($X_{\mathrm{CO}} \sim 3.6$; Daddi et al. 2010). Using a larger value for X_{CO} would produce gas masses 4.5 times larger than quoted here. From the CO luminosities found in the previous section, we find $M_{\mathrm{gas}} = (3.2 \pm 0.5) \times 10^{10}(\mu/15)^{-1}(X_{\mathrm{CO}}/0.8)$ and $(1.7 \pm 0.3) \times 10^{10}(\mu/20)^{-1}(X_{\mathrm{CO}}/0.8)\,\mathrm{M}_\odot$ for SPT 2332−53 and SPT 0538−50, respectively.

We compute dynamical masses for our sources based on the CO line profiles. For a disc gas distribution, the dynamical mass of the system is given by $M_{\mathrm{dyn}} \approx 2.3 \times 10^5\ \Delta v^2_{\mathrm{FWHM}}\ R\ \sin^{-2}(i)\ \mathrm{M}_\odot$, where Δv_{FWHM} is the observed CO line full-width half-maximum (FWHM) in units of km s^{-1}, R is the disc radius in kpc and i is the inclination angle. For a merger model, Δv_{FWHM} represents half the physical separation in velocity of the component CO lines and R is half the separation between components (Solomon & Vanden Bout 2005).

Given the poor constrains on the geometries of both sources, we derive dynamical masses by adopting disc geometries. For SPT 2332−53, we use $R = 2$ kpc and an average inclination angle $i \sim 57^\circ$ (Law et al. 2009), which yields $M_{\mathrm{dyn}} = 7.8 \times 10^{10}\,\mathrm{M}_\odot$. This implies a gas fraction of ∼0.4 for $\mu = 15$ and the adopted X_{CO} value. For SPT 0538−50, we use $R = 1.6$ kpc (from the lens model), a CO profile FWHM of ∼500 km s^{-1} (from the full CO line) and an average inclination $i \sim 57^\circ$, yielding $M_{\mathrm{dyn}} = 1.3 \times 10^{11}\,\mathrm{M}_\odot$. This leads to a gas fraction of ∼0.1 for $\mu = 20$ and the adopted X_{CO}. We remark that since the actual source geometries are unknown, the estimated dynamical masses and gas fractions are uncertain and should be taken with caution as they are given for reference only.

4.3 Star formation efficiencies and depletion time-scales

The star formation efficiency (SFE) can be defined as SFE = $L_{\mathrm{IR}}/L'_{\mathrm{CO}}$ in units of L$_\odot$ (K km s^{-1} pc^2)$^{-1}$. From this, we obtain SFEs of 110 and 205 L$_\odot$ (K km s^{-1} pc^2)$^{-1}$ for SPT 2332−53 and SPT 0538−50, respectively. The gas depletion time-scale can be defined as $t_{\mathrm{dep}} = M_{\mathrm{gas}}/\mathrm{SFR}$. We adopt SFR (M$_\odot$ yr^{-1}) = $1.5 \times 10^{-10}\,L_{\mathrm{IR}}$ (L$_\odot$) (Murphy et al. 2011) for consistency with Greve et al. (2012). This yields gas depletion time-scales of $\sim 4.9 \times 10^7(\mu/15)^{-1}(X_{\mathrm{CO}}/0.8)$ and $\sim 2.6 \times 10^7(\mu/20)^{-1}(X_{\mathrm{CO}}/0.8)$ yr for SPT 2332−53 and SPT 0538−50, respectively. While values for the depletion time-scales for DSFGs and local ULIRGs are typically $<10^8$ yr (e.g. Greve et al. 2005; Solomon & Vanden Bout 2005), distant 'normal' star-forming disc galaxies were found to have depletion time-scales of $\sim(0.3-2) \times 10^9$ yr (Daddi et al. 2010; Tacconi et al. 2010, 2012). The depletion time-scales for our sources appear to be consistent with typical DSFGs and local ULIRGs.

4.4 SPT 0538−50: free–free, synchrotron and dust emission

SPT 0538−50 is additionally detected at 2.2 and 5.5 GHz by ATCA. At $z = 2.783$ the 2.2, 5.5, 30.6 and 35 GHz observations sample 8.3, 20.8, 115.7 and 132.4 GHz in the rest frame, respectively, providing a long lever arm to measure the radio spectral index of the source.

Fig. 3 shows the recently obtained ATCA 5.5 GHz continuum image towards SPT 0538−50. The image structure matches the position and structure of the Einstein ring found in the ALMA images (Hezaveh et al. 2013), clear evidence that the bulk of the radio emission comes from the lensed background source. We thus rule out the foreground galaxy contribution to the radio emission based on the morphology shown by ALMA and ATCA.

In the following section, we analyse the radio spectral properties of SPT 0538−50 and adopt the rest-frame frequencies for clarity. We define the flux density S_ν in terms of the observed frequency ν as $S_\nu \propto \nu^\alpha$, with α the radio spectral index. The data seem to

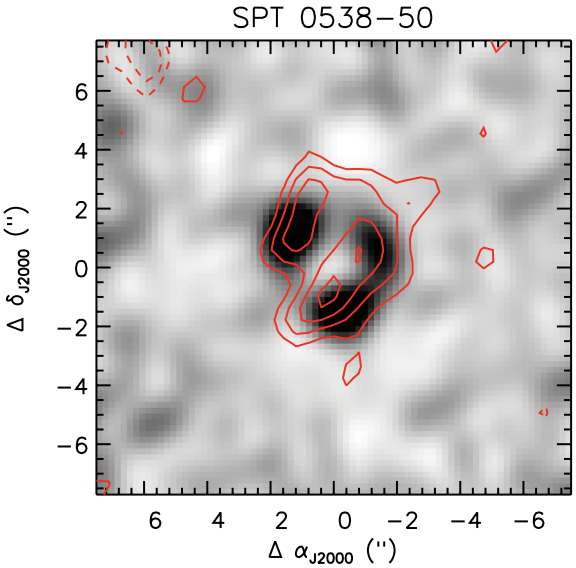

Figure 3. The ALMA 345 GHz high-resolution map for SPT 0538−50 is shown in the background (Hezaveh et al. 2013) with red contours overlaid representing the ATCA 5.5 GHz radio map. Contour levels are in steps of $\pm 1\sigma$, starting at $\pm 2\sigma$ with $\sigma = 35$ μJy beam^{-1}. The spatial coincidence between the submillimetre and radio emission confirms that the latter arises from the background lensed object.

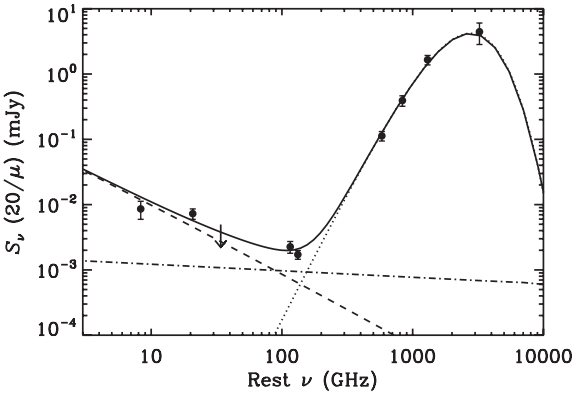

Figure 4. The radio-to-IR spectrum of SPT 0538−50 fitted by a combination of modelled radio and IR spectra (solid line). Photometry is shown with error bars, along with an upper limit at $\nu_{\rm rest} = 25$ GHz. The IR dust emission is given by a grey-body model (dotted line). The radio spectrum is modelled by two components, non-thermal synchrotron emission (long-dashed lines) and thermal, free–free emission (dot–dashed line).

suggest that the radio spectrum may steepen between rest-frame 8.3 and 132.4 GHz as the observed spectral index between 8.3 and 20.8 GHz is -0.18 ± 0.39, and -0.76 ± 0.11 between 20.8 and 132.4 GHz (see Fig. 4). In fact, subtracting off an estimate of the thermal dust contribution to the 132.4 GHz flux density suggests an even steeper intrinsic (free–free + synchrotron) radio spectral index between 20.8 and 132.4 GHz of -0.89 ± 0.14. Given the large uncertainties on the photometry, we do not include an additional free parameter for spectral curvature in our fit to the radio spectrum, and simply assume a single power law without a break. However, we consider and discuss the physical implications of the observed spectral flattening at lower frequencies below in Section 4.4.3.

4.4.1 Fitting the radio-to-IR spectrum: free–free emission and an independent SFR estimate

To estimate the amount of free–free emission at rest-frame 115.7 and 132.4 GHz, which can then be used to calculate an SFR, we fit the full radio-to-IR spectrum. For simplicity, we use the grey-body fit from Greve et al. (2012) to model the thermal dust component, which has a fixed emissivity spectral index $\beta = 2$. To fit the radio spectrum, we vary a combination of free–free (thermal) and synchrotron (non-thermal) radio emission components which scale as $S_\nu^{\rm T} \propto \nu^{\alpha_{\rm T}}$ and $S_\nu^{\rm NT} \propto \nu^{\alpha_{\rm NT}}$, respectively, where $\alpha_{\rm T} = -0.1$ and $\alpha_{\rm NT}$ are the free–free and synchrotron spectral indices, respectively.

Before varying the free–free and synchrotron components to fit the observed radio spectrum, we first need to assume a non-thermal spectral index. We assume a synchrotron spectral index of $\alpha_{\rm NT} = -1.0$, which is consistent with the steepest part of the radio spectrum measured between 20.8 and 132.4 GHz (see above). This value is in agreement with an estimate for the non-thermal spectrum based on the calculation of energy losses to cosmic ray electrons in this system arising from synchrotron radiation, inverse Compton scattering, ionization, bremsstrahlung and escape through an empirical prescription (see Murphy 2009 for details). Furthermore, this value is consistent with the synchrotron spectral index of -1.05 ± 0.05 for two DSFGs at $z \sim 2.5$ found by Thomson et al. (2012). Setting $\alpha_{\rm NT} = -1.0$, our best-fitting model to the radio-to-IR data suggests a free–free radio fraction at 115.7 and 132.4 GHz of 42 ± 10 and 55 ± 13 per cent, respectively (see Fig. 4).

Taking these values and the free–free SFR calibration given in Murphy et al. (2012) results in an SFR $= 470 \pm 170\,{\rm M}_\odot\,{\rm yr}^{-1}$. This is consistent with the IR-luminosity-derived estimate of SFR $= 650 \pm 100\,{\rm M}_\odot\,{\rm yr}^{-1}$, which is again calculated using the calibration given in Murphy et al. (2011), calibrated for a common initial mass function (IMF; i.e. Kroupa 2001), and consistent with the estimate from Greve et al. (2012). We note that such calibrations between IR luminosity and SFR are not likely accurate to better than a factor of 2 (Kennicutt 1998; Omont et al. 2001), and this uncertainty is not included in the error above on the IR-derived SFR.

4.4.2 Physical considerations in the fitting

While we have assumed a physically motivated value for the non-thermal spectral index, it is worth noting that this assumed value is marginally inconsistent with a naive measurement of α from our data. Using an ordinary least-squares fit to the four radio detections, weighted by the uncertainties of the flux density measurements, results in a radio spectral index (before correcting for thermal dust emission) of $\alpha = -0.65 \pm 0.10$. Assuming this value for the non-thermal radio spectral index, the fit results in a 132.4 GHz free–free fraction of ∼2 per cent. Similarly, using a dust emissivity index $\beta = 2$ and a radio spectral index ∼0.75 (Ibar et al. 2010) would result in a free–free fraction of ∼20 per cent.

For any physical configuration in which most of the IR emission is powered by star formation, such a small fraction of free–free radio emission is highly unlikely. A situation without free–free emission could arise for cases where: (a) the emission is purely powered by an AGN; (b) there is a suppression of Lyman continuum photons, and thus free–free emission, through an upper mass cutoff of the IMF at $\sim 20\,{\rm M}_\odot$ while still providing synchrotron emission from supernovae ($\sim$8–20 M$_\odot$); and (c) the absorption of ionizing photons by dust in the actual starburst. However, the galaxy shows a rather normal, albeit slightly higher, IR/radio ratio (see Section 4.4.3), which is difficult to keep constant if there are

variations in the IMF or in the presence of a powerful AGN. In the case where dust successfully competes with neutral hydrogen for ionizing photons, we still expect a significant free–free component to be present and compatible with the amount of ongoing star formation inferred from the IR spectrum (Murphy et al. 2012). A similar situation has been observed in local (U)LIRGs, where the synchrotron spectrum is found to be increasingly depressed at high frequencies (e.g. Clemens et al. 2008; Leroy et al. 2012), perhaps arising from a modified electron injection spectrum in such dense starbursts.

4.4.3 Spectral flattening due to a deeply embedded compact starburst

The radio observations suggest that the radio spectrum flattens towards lower frequencies. This flattening may be the result of the radio continuum emission becoming optically thick at lower frequencies, as observed in local compact ULIRGs (Condon et al. 1991). Indeed, the lens model of SPT 0538−50 indicates the presence of an IR-dominant, compact source. Such a spectral flattening at lower radio frequencies typically causes sources to have IR/radio (1.4 GHz) ratios that are larger than the average value among star-forming galaxies (Condon et al. 1991). Extrapolating a 1.4 GHz flux density using the observed rest-frame 8.3 GHz flux density along with the spectral index measured between 8.3 and 20.8 GHz suggests that the galaxy has a logarithmic IR/1.4 GHz ratio $q_{\rm IR} = 2.84$.[1] This implies a linear ratio nearly 60 per cent (1σ) larger than the average value of $q_{\rm IR} = 2.64 \pm 0.02$ found for local star-forming galaxies with 1.4 GHz luminosities in the range $\sim 10^{19}$–$10^{24.5}$ W Hz^{-1}(Bell 2003).

Assuming that the spectral flattening is in fact the result of the source being powered by an optically thick starburst, we can use local relations to infer properties of the galaxy. Recently, Murphy et al. (2013) found a correlation between the radio spectral index of $z \sim 0$ (U)LIRGs and their distance from the star-forming main sequence (i.e. specific SFR defined as sSFR = SFR/$M_\star$). That is, galaxies having flatter spectral indices, most likely due to harbouring compact starbursts, which are optically thick at low radio frequencies, have increasingly higher sSFRs. Based on this correlation, and assuming an evolution in the sSFR of galaxies from $z \sim 0$ to $z \sim 3$, where the typical sSFR at $z \sim 3$ is 4.5 Gyr^{-1} (Karim et al. 2011), the spectral index measured between 8.3 and 20.8 GHz suggests that the sSFR of SPT 0538−50 is $\sim 10.2 \pm 2.9$ Gyr^{-1}, more than a factor of $\sim$2 above the $z \sim 3$ main sequence for star-forming galaxies (Karim et al. 2011). Taking the above free–free estimate for the SFR suggests that this system has $M_\star = (4.6 \pm 2.1) \times 10^{10}\,{\rm M}_\odot$.

5 DISCUSSION AND SUMMARY

We have obtained sensitive CO(1–0) and radio continuum ATCA observations towards two bright DSFGs discovered in millimetre survey data taken with the SPT. This corresponds to a pilot study of a larger sample of millimetre bright SPT sources with available spectroscopic redshifts.

[1] The latter is defined as the ratio of the total IR luminosity (8–1000 μm) to the radio power:

$$q_{\rm IR} = \log_{10}\left(\frac{L_{\rm IR}}{3.75 \times 10^{12}\ {\rm W\ m^{-2}}}\right) - \log_{10}\left(\frac{S_{1.4\ {\rm GHz}}}{{\rm W\ m^{-2}\ Hz^{-1}}}\right).$$

Both systems are found to be rich in molecular gas with masses $\sim 2 \times 10^{10}\,{\rm M}_\odot$, gas fractions of $\sim$0.1–0.4 and SFEs of $\sim$100–200 ${\rm L}_\odot$ (K km s^{-1} pc^2)$^{-1}$, for the adopted values of the magnification (μ) and CO luminosity to gas mass conversion factor ($X_{\rm CO}$). Taken together, the observed CO properties are compatible with those found in other lensed (and unlensed) submillimetre-selected galaxies based on previous CO(1–0) measurements (Harris et al. 2010; Frayer et al. 2011; Ivison et al. 2011).

In both cases, we find $\sim$31 and 35 GHz continuum detections in the field (rest-frame 115.7 and 132.4 GHz). While in the case of SPT 2332−53 the continuum emission comes from the foreground BCG, in the case of SPT 0538−50 the radio emission is clearly identified with the CO source, as shown in Fig. 3. Assuming a non-thermal spectral index of $\alpha_{\rm NT} = -1.0$, our modelling of the radio-to-IR spectrum of SPT 0538−50 suggests that 42 ± 10 and 55 ± 13 per cent of the emission at rest-frame 115.7 and 132.4 GHz arises from a free–free component. This allows us to derive a free–free SFR value of $470 \pm 170\,{\rm M}_\odot\ {\rm yr}^{-1}$, which is consistent within the uncertainties with the IR-derived SFR. Recently, Thomson et al. (2012) detected CO(1–0) line emission in three submillimetre-selected galaxies at $z \sim 2.5$–2.9, and marginally detected the rest-frame 115 GHz continuum from two of these galaxies. Their modelling of the radio spectra indicates free–free contributions to the rest-frame 115 GHz in the range $\sim$30–40 per cent (Thomson et al. 2012). This is similar to our results, which are based on significant detections at rest-frame 115.7 and 132.4 GHz on SPT 0538−50.

Analysis of the radio spectral curvature for this source suggests that the star formation activity is powered by a compact starburst; the spectral flattening towards lower radio frequencies is similar to what is observed for local (U)LIRGs harbouring compact starbursts that become optically thick at low radio frequencies. From this analysis, we estimate a stellar mass of $(4.6 \pm 2.1) \times 10^{10}\,{\rm M}_\odot$. It is interesting to note that almost all local ULIRGs are powered by merger-driven star formation and lie above the star-forming main sequence, which also seems to be the case for SPT 0538−50 with an sSFR of 10.2 Gyr^{-1} compared to the main sequence at $z \sim 3$ with an average sSFR of 4.5 Gyr^{-1}. Furthermore, the ULIRG-like nature of this source is supported by the results from the lens model which indicate that SPT 0538−50 is composed of a compact IR-dominant component, which comprises 70 per cent of the IR luminosity (Hezaveh et al. 2013). This is similar to what is seen in local ULIRGs (Bryant & Scoville 1999).

These results exemplify the use of deep low-J CO spectroscopy in high-redshift star-forming galaxies taking advantage of the large bandwidths available with ATCA and the Karl Jansky Very Large Array. The advent of important samples of bright, gravitationally lensed galaxies from the SPT and *Herschel* surveys makes possible detailed studies of the ISM in DSFGs. While the observation of the CO line emission enables a direct measurement of the gas and dynamical masses, modelling of the radio spectrum enables independent measurements of the SFRs and stellar masses without the need of near-to-far-IR imaging, which generally requires space-based observatories.

ACKNOWLEDGEMENTS

We thank Andy Biggs for useful discussions. MA and this work was co-funded under the Marie Curie Actions of the European Commission (FP7-COFUND). The Australia Telescope is funded by the Commonwealth of Australia for operation as a National Facility managed by CSIRO. The SPT is supported by the National

Science Foundation through grant ANT-0638937, with partial support through PHY-1125897, the Kavli Foundation and the Gordon and Betty Moore Foundation.

REFERENCES

Amblard A. et al., 2011, Nat, 470, 510
Aravena M. et al., 2010, ApJ, 708, L36
Barvainis R., Antonucci R., Coleman P., 1992, ApJ, 399, L19
Bell E. F., 2003, ApJ, 586, 794
Blain A. W., Smail I., Ivison R. J., Kneib J.-P., Frayer D. T., 2002, Phys. Rep., 369, 111
Brodwin M. et al., 2008, ApJ, 687, L65
Brown R. L., Vanden Bout P. A., 1991, AJ, 102, 1956
Brown R. L., Vanden Bout P. A., 1992, ApJ, 397, L11
Bryant P. M., Scoville N. Z., 1999, AJ, 117, 2632
Capak P. L. et al., 2011, Nat, 470, 233
Carlstrom J. E. et al., 2011, PASP, 123, 568
Chapman S. C., Blain A. W., Smail I., Ivison R. J., 2005, ApJ, 622, 772
Clemens M. S., Vega O., Bressan A., Granato G. L., Silva L., Panuzzo P., 2008, A&A, 477, 95
Condon J. J., Huang Z.-P., Yin Q. F., Thuan T. X., 1991, ApJ, 378, 65
Daddi E. et al., 2009, ApJ, 694, 1517
Daddi E. et al., 2010, ApJ, 713, 686
Downes D., Solomon P. M., 1998, ApJ, 507, 615
Frayer D. T., Ivison R. J., Scoville N. Z., Yun M., Evans A. S., Smail I., Blain A. W., Kneib J.-P., 1998, ApJ, 506, L7
Frayer D. T. et al., 2011, ApJ, 726, L22
Genzel R. et al., 2012, ApJ, 746, 69
Greve T. R., Ivison R. J., Papadopoulos P. P., 2003, ApJ, 599, 839
Greve T. R. et al., 2005, MNRAS, 359, 1165
Greve T. R. et al., 2012, ApJ, 756, 101
Harris A. I., Baker A. J., Zonak S. G., Sharon C. E., Genzel R., Rauch K., Watts G., Creager R., 2010, ApJ, 723, 1139
Hezaveh Y. D. et al., 2013, ApJ, 767, 132
Ibar E., Ivison R. J., Best P. N., Coppin K., Pope A., Smail I., Dunlop J. S., 2010, MNRAS, 401, L53
Ivison R. J., Smail I., Le Borgne J.-F., Blain A. W., Kneib J.-P., Bezecourt J., Kerr T. H., Davies J. K., 1998, MNRAS, 298, 583
Ivison R. J., Papadopoulos P. P., Smail I., Greve T. R., Thomson A. P., Xilouris E. M., Chapman S. C., 2011, MNRAS, 412, 1913
Karim A. et al., 2011, ApJ, 730, 61
Kennicutt R. C., Jr, 1998, ARA&A, 36, 189
Kroupa P., 2001, MNRAS, 322, 231
Lagache G., Puget J.-L., Dole H., 2005, ARA&A, 43, 727
Law D. R., Steidel C. C., Erb D. K., Larkin J. E., Pettini M., Shapley A. E., Wright S. A., 2009, ApJ, 697, 2057
Leroy A. K. et al., 2012, AJ, 144, 3
McMullin J. P., Waters B., Schiebel D., Young W., Golap K., 2007, in Shaw R. A., Hill F., Bell D. J., eds, ASP Conf. Ser. Vol. 376, Astronomical Data Analysis Software and Systems XVI. Astron. Soc. Pac., San Francisco, p. 127
Murphy E. J., 2009, ApJ, 706, 482
Murphy E. J. et al., 2011, ApJ, 737, 67
Murphy E. J. et al., 2012, ApJ, 761, 97
Murphy E. J., Stierwalt S., Armus L., Condon J. J., Evans A. S., 2013, ApJ, 768, 2
Negrello M. et al., 2010, Sci, 330, 800
Omont A., 2007, Rep. Prog. Phys., 70, 1099
Omont A., Cox P., Bertoldi F., McMahon R. G., Carilli C., Isaak K. G., 2001, A&A, 374, 371
Papadopoulos P. P., Ivison R. J., 2002, ApJ, 564, L9
Pilbratt G. L. et al., 2010, A&A, 518, L1
Riechers D. A., Hodge J., Walter F., Carilli C. L., Bertoldi F., 2011, ApJ, 739, L31
Rowan-Robinson M. et al., 1991, Nat, 351, 719
Sault R. J., Teuben P. J., Wright M. C. H., 1995, in Shaw R. A., Payne H. E., Hayes J. J. E., eds, ASP Conf. Ser. Vol. 77, Astronomical Data Analysis Software and Systems IV. Astron. Soc. Pac., San Francisco, p. 433
Solomon P. M., Vanden Bout P. A., 2005, ARA&A, 43, 677
Swinbank A. M. et al., 2010, Nat, 464, 733
Tacconi L. J. et al., 2010, Nat, 463, 781
Tacconi L. J. et al., 2013, ApJ, 768, 64
Thomson A. P. et al., 2012, MNRAS, 425, 2203
Vieira J. D. et al., 2010, ApJ, 719, 763
Vieira J. D. et al., 2013, Nat, 495, 344
Viero M. P. et al., 2009, ApJ, 707, 1766
Weiss A. et al., 2013, ApJ, 767, 88

This paper has been typeset from a TEX/LATEX file prepared by the author.